geosciences

MDPI

Article

Neural Network Inversion Algorithm for Geostress Field Based on Physics-Informed Constraints

Fei Li [1,2,*], Lin Wang [1], Zhifeng Liang [1], Jinan Wang [1], Chuanqi Zhu [3] and Ruiyang Yuan [4]

[1] School of Resources and Safety Engineering, University of Science and Technology Beijing, Beijing 100083, China; m202320189@xs.ustb.edu.cn (L.W.); zliang@srk.com (Z.L.); wjarock@ces.ustb.edu.cn (J.W.)
[2] National Technological Innovation Center for Efficient Development of Strategic Rare Metal Mineral Resources, Beijing 100083, China
[3] State Key Laboratory of Digital Intelligent Technology for Unmanned Coal Mining, Anhui University of Science and Technology, Huainan 232001, China; cqzhu@aust.edu.cn
[4] CCTEG Shenyang Research Institute, Shenyang 110141, China; yuanruiyang@syccri.com
* Correspondence: lifei2016@ustb.edu.cn

Abstract

Traditional methods for geostressfield inversion face issues such as weak physical interpretability and insufficient generalization ability. This study pioneers the application of Physics-Informed Neural Network (PINN) to this problem, developing a data- and physics-driven inversion algorithm. The framework incorporates a constitutive-equation-based regularized loss function as a hard constraint during training to ensure physical consistency. To address boundary load uncertainty, two quantification approaches—Bayesian linear regression and surrogate model optimization—are proposed to establish 95% confidence intervals for boundary coefficients. Verification based on simple three-dimensional models and actual geological models of mines shows that PINN inversion achieves a mean absolute relative error as low as 0.0772%, with an error of 15.67% under sparse sampling conditions—significantly lower than the 31.07% error of the traditional Back propagation neural network. This demonstrates excellent robustness and data efficiency. In the practical engineering application of complex geological bodies, the average error of principal stress inversion is 9.35% with a minimum error of 0.137%. All inversion results fall within the permissible accuracy range of engineering, and the stress distribution conforms to basic laws, with an average error of 0.453 in the constitutive relation. Compared with BP neural network and multiple linear regression methods, it shows obvious accuracy advantages. This method provides a new solution for intelligent ground stress prediction with high accuracy, high efficiency, and strong physical interpretability, and also lays the foundation for early identification of geological disasters.

Keywords: initial in situ stress field; inversion analysis; physics-informed neural network (PINN)

Check for updates

Academic Editors: Xiangchao Shi, Zetian Zhang and Daobing Wang

Received: 21 January 2026
Revised: 4 March 2026
Accepted: 9 March 2026
Published: 12 March 2026

Copyright: © 2026 by the authors. Licensee MDPI, Basel, Switzerland. This article is an open access article distributed under the terms and conditions of the Creative Commons Attribution (CC BY) license.

1. Introduction

The initial in situ stress field serves as the foundation for stability analysis in geotechnical engineering, early warning of geological hazards, and resource exploration and development [1]. Its accurate reconstruction is crucial for revealing the mechanical response of rock masses under engineering disturbances, optimizing engineering design, and ensuring construction safety [2,3]. However, the in situ stress field is affected by the

coupling of multiple factors such as geological structures, lithological combinations, and topography, making it difficult to directly obtain the full-field stress distribution relying solely on limited on-site measured data. Therefore, reconstructing the in situ stress field through methods such as numerical simulation and inversion analysis has become a research focus.

At present, both domestic and international research on initial in situ stress field inversion has achieved significant results. Early studies were largely based on linear regression theory, employing regression analysis by superimposing multiple tectonic stress field functions [4], or simplifying rock masses as homogeneous linear elastic media and iteratively adjusting boundary loads to align numerical model outputs with measured data points [5]. While such methods offer clear physical conceptualization, they often face limitations in accuracy and generalization capability when dealing with complex geological conditions due to oversimplified constitutive models (neglecting rock mass nonlinearity, anisotropy, time-dependent effects, etc.) [6]. In recent years, data-driven approaches represented by machine learning (e.g., BP neural networks [7], support vector machines [8]) and deep learning (e.g., generative adversarial networks [9], long short-term memory networks [10]) have been introduced into the field of in situ stress inversion. These methods can uncover complex nonlinear mapping relationships from geological and measured data without constructing explicit physical equations, demonstrating excellent fitting and predictive capabilities under specific conditions [11,12]. However, purely data-driven models are inherently "black-box" in nature, and their predictions may violate fundamental physical laws (such as equilibrium equations and compatibility conditions), resulting in poor physical interpretability [13,14]. More importantly, such models rely on large volumes of high-quality, well-distributed training samples. In scenarios where measured data from deep engineering projects are scarce, they are prone to overfitting and poor extrapolation reliability, which limits their broader application in engineering practice [15,16].

To bridge the gap between purely physical models and purely data-driven models, Physics-Informed Neural Networks (PINN) have emerged [17,18]. The core innovation of PINNs lies in embedding the physical laws governing the problem—typically expressed as partial differential equations or algebraic equations—as soft constraint terms into the loss function of the neural network, thereby constructing a modeling paradigm that integrates "data-driven" and "physics-driven" approaches [19]. This method has demonstrated significant potential across various fields of scientific computing and engineering inversion, such as solving the Eikonal equation [20], reconstructing flow fields from sparse data in fluid dynamics [21], inferring thermal parameters in heat conduction problems [22–25], solving seismic wave propagation equations in geophysics [26], and addressing inverse problems in nanophotonics [27]. These successful cases indicate that PINN, through "physics-based regularization," strongly constrains the solution space, ensuring physical consistency of solutions even with limited training data, while significantly enhancing the model's generalization capability and interpretability [28]. This provides a novel pathway to resolve the conflict between data scarcity and physical constraints in in situ stress inversion.

This study addresses the challenges of weak physical constraints and strong data dependence in in situ stress inversion by proposing a "data-physics" dual-driven inversion method based on PINN. By incorporating linear elastic constitutive relationships as soft constraints into the loss function, the physical consistency of the inversion results is ensured. Additionally, Bayesian linear regression and surrogate model optimization are combined to quantify boundary load uncertainties, enhancing the robustness and interpretability of the inversion. The strongly physics-constrained inversion framework, established under linear elastic theory, validates the effectiveness of the physical embedding mechanism and

provides a methodological foundation for integrating more complex constitutive models in future work.

2. Physics-Informed Neural Network Inversion Algorithm

Physics-Informed Neural Network (PINN) is a machine learning model that combines deep learning and physics knowledge. Different from traditional data-driven neural networks, PINN uses physical laws to guide the model during the learning process to improve the model's generalization ability. In PINN, the neural network is divided into a main network and a physical network: the main network is used to fit the mapping relationship between input and output, while the physical network is used to represent physical laws. The training process combines the two networks, and the calculation process of PINN is shown in Figure 1.

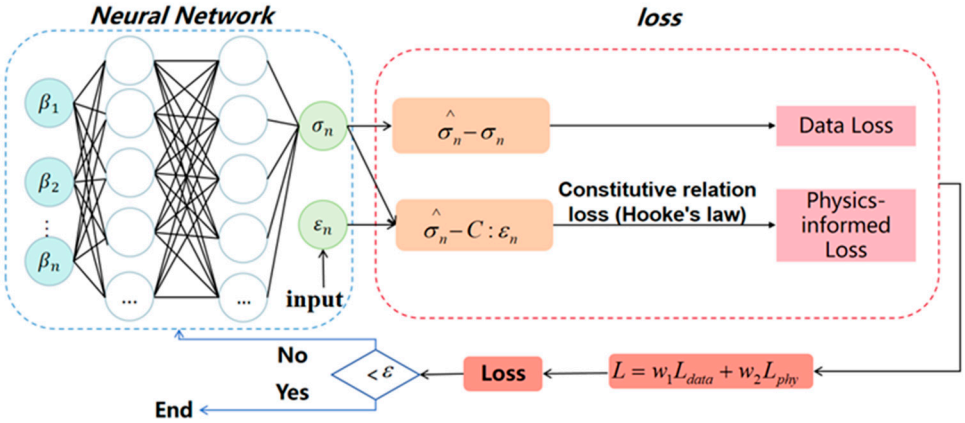

Figure 1. Flowchart of Physics-Informed Neural Network.

The main network consists of an input layer, hidden layers, and an output layer, with forward propagation implemented through multiple hidden layers. The loss function comprises two components: data loss and Physics-informed Loss. The data loss, measured by mean squared error (Equation (1)), quantifies the deviation between predicted outputs and observed data, aiming to fit the data. The Physics-informed Loss serves as a regularization term unique to PINN, ensuring the physical consistency of the solution by computing residuals from physical equations. The two loss components are combined via weighted summation to form the total loss function, allowing optimal balance between data fitting and physical constraints through weight adjustment.

$$MSE = \frac{1}{N}\sum_{i=1}^{N}(y_i - \hat{y}_i)^2 \quad (1)$$

To verify the correctness and applicability of the in situ Stress Field Inversion Algorithm based on PINN, this paper conducts in situ stress field inversion using this algorithm, and the specific process is shown in Figure 2.

First, a simplified three-dimensional model of the stratigraphy in the inversion area is established using ABAQUS 2022 software, with stress boundary conditions determined based on the geological survey report. The 95% confidence intervals for the boundary coefficients are then calculated using either Bayesian linear regression or surrogate model optimization. Within these intervals, 50 sets of samples are generated via uniform sampling design. Based on these samples, the main network is constructed, and both the data loss and Physics-informed Loss functions are defined to formulate the PINN model. The actual stress field distribution of the area is obtained as the set of stress–strain data that minimizes the total loss function through network training.

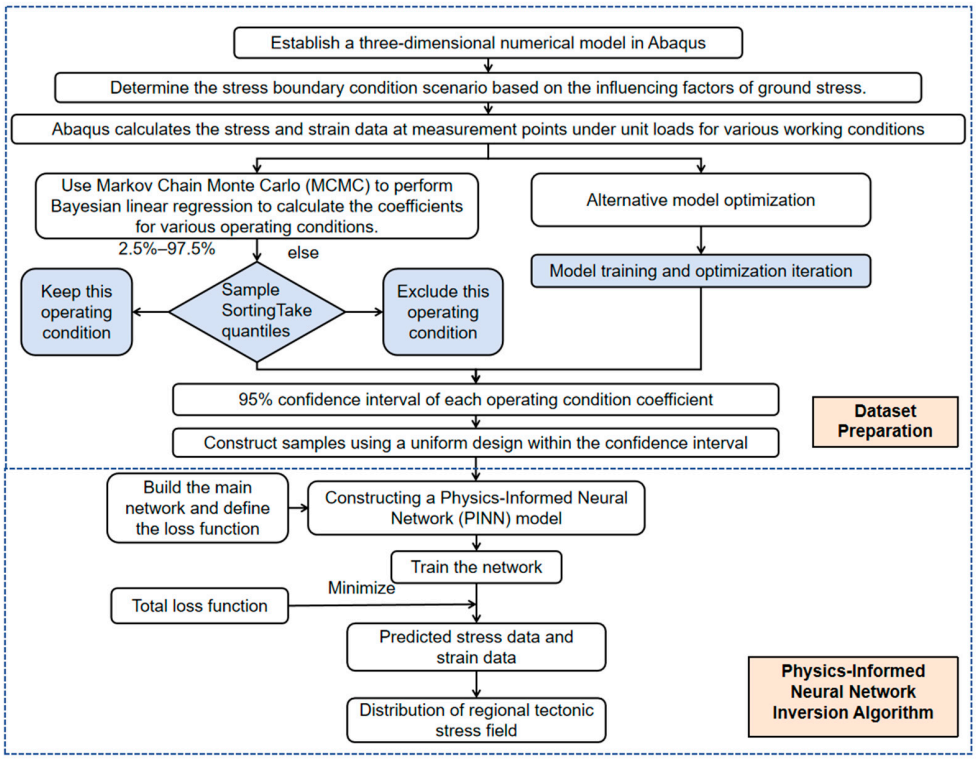

Figure 2. Flowchart of in situ Stress Field Inversion Algorithm Based on Physics-Informed Neural Network (PINN).

2.1. Influencing Factors of the Initial In Situ Stress Field

The initial in situ stress is predominantly governed by gravitational forces and tectonic movements, and the corresponding stress field can be characterized as a superposition of the gravitational stress field and the tectonic stress field [29,30], as shown in Equation (2).

$$\sigma^{in-situ} = \sigma^{g} + \sigma^{t} \tag{2}$$

where $\sigma^{in-situ}$ is the initial stress field; σ^{g} and σ^{t} are the gravitational stress field and the tectonic stress field, respectively.

Based on this, nine influencing factors are selected for the study: gravitational stress, lateral (Y-direction) compressive tectonic movement, longitudinal (X-direction) compressive tectonic movement, horizontal shear tectonic movement, and vertical shear tectonic movement. Among these, the latter four types of tectonic movements each encompass two working conditions, corresponding to loads applied on the right-side interface and the rear interface of the geological model, respectively.

2.2. Determination of Confidence Intervals for Each Working Condition

2.2.1. Bayesian Linear Regression Method

Bayes' theorem combines prior knowledge with observed data to obtain the posterior probability distribution of parameters [31,32]. In the initial in situ stress field inversion, the initial in situ stress field can be regarded as a linear superposition of the above nine working conditions. Therefore, the Bayesian linear regression model is assumed as shown in Equation (3).

$$Y = X\beta + \varepsilon \tag{3}$$

where Y is the dependent variable vector (measured stress value), X is the independent variable vector (stress value under unit load of each working condition), β is the regression coefficient vector (load coefficient value of each working condition), and ε is the error vector.

According to Bayesian theory, the observed data Y is usually assumed to follow a Gaussian distribution with mean $X\beta$ and covariance $\sigma^2 I$. The likelihood function is shown in Equation (4). The marginal probability distribution $P(Y|X)$ is calculated by integrating β and σ^2, as shown in Equation (5).

$$P\left(Y\middle|X,\beta,\sigma^2\right) = N\left(Y\middle|X\beta,\sigma^2 I\right) = \frac{1}{(2\pi\sigma^2)^{N/2}} \exp\left(-\frac{\sum_{i=1}^{N}\left(y_i - x_i^T\beta\right)^2}{2\sigma^2}\right) \tag{4}$$

$$P(Y|X) = \int P\left(Y\middle|X,\beta,\sigma^2\right)P\left(\beta,\sigma^2\right)d\beta d\sigma^2 \tag{5}$$

Determination of 95% Confidence Interval

Subsequently, MATLAB code is written to use the Markov Chain Monte Carlo (MCMC) method (specifically the Gibbs sampling algorithm) to estimate the posterior distribution of parameters in the probability space [33,34]. The specific process is shown in Figure 3. Thus, the arithmetic mean and 95% confidence interval of each working condition coefficient can be directly obtained.

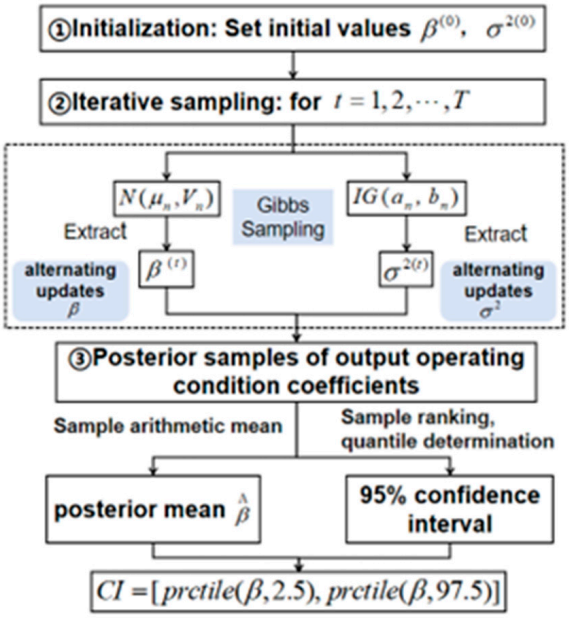

Figure 3. Flowchart of MCMC estimating parameter posterior distribution via Gibbs sampling.

Setting Prior Distribution and Posterior Distribution

The prior distribution of regression coefficients is set as shown in Equation (6), and the prior distribution of error variance is set as shown in Equation (7). And the posterior distribution can be obtained from the conditional posterior distribution and the marginal posterior distribution, as shown in Equation (8):

$$\beta \sim N(\mu_0, V_0) \tag{6}$$

$$\sigma^2 \sim IG(a, b) \tag{7}$$

$$P\left(\beta,\sigma^2\middle|X,Y\right) = P\left(\beta\middle|\sigma^2,X,Y\right)\cdot P\left(\sigma^2\middle|X,Y\right) \tag{8}$$

where $\mu_0 = 0$, $V_0 = 100I$, $a = 1$, $b = 1$.

2.2.2. Surrogate Model Optimization Method

The core of this method is to generate an "optimal solution set" through multiple optimization iterations, treat this set as statistical samples [35] and then calculate the confidence interval for each parameter (working condition coefficient) based on the t-distribution.

Establishment of Initial Sample Library

The constraint range $[C_{\min}, C_{\max}]$ of each working condition coefficient is determined based on prior geological experience, and N groups of initial working condition coefficient combinations are generated using the Latin Hypercube Sampling (LHS) technique. LHS is a stratified random sampling method that ensures uniform distribution of samples in the parameter space. Based on the linear superposition principle, each group of coefficient combinations is multiplied by the pre-calculated unit load working condition response matrix to synthesize the corresponding overall stress response R_{sim}, as shown in Equation (9):

$$R_{\text{sim}} = \sum_{j=1}^{9} (C_j \cdot U_j) \tag{9}$$

where C_j is the to-be-inverted coefficient of the j-th load working condition; U_j is the unit stress response generated by the j-th unit load working condition.

Construct the initial dataset: Combine the generated coefficient combinations (input) and calculated stress responses (output) into sample pairs $\{C_i, R_i\}$ to form the initial training dataset D.

Surrogate Model Training and Optimization Iteration

A Feed-Forward Neural Network (FFNN) is trained on dataset D, with working condition coefficients as input and stress responses as output. This network serves as a surrogate model for fast approximate linear superposition calculations. Taking the on-site measured stress response R_{measured} as the target, the trained surrogate model is used to predict the stress, and the Root Mean Square Error (RMSE) between the predicted value and the measured value is used as the fitness function to drive the Genetic Algorithm (GA) for global search, finding the optimal working condition coefficient combination C_t under the current surrogate model. The optimal solution C_t obtained in this optimization is used as a new sample point, its corresponding accurate physical response (linear superposition) is calculated, and this new sample pair is added to the training dataset D. Sample points in promising areas are added to the training set to guide the surrogate model to continuously improve accuracy near the optimal solution. Finally, adaptive sampling is performed, i.e., the above steps (retraining the surrogate model $\rightarrow$ optimization $\rightarrow$ sample expansion) are repeated iteratively until the maximum number of iterations or the error convergence tolerance is met [36].

Calculation of 95% Confidence Interval

First, construct the optimal solution sample set: Record the optimal solutions $C_{t1}, C_{t2}, \ldots, C_{tM}$ (where M is the number of effective iterations) found by the genetic algorithm in each iteration. This set represents the possible distribution of optimal parameters under the influence of inversion problem uncertainty. Then, for each working condition coefficient, calculate the sample mean $\overline{x}_j$ and sample standard deviation S_j from its optimal solution set. Due to the limited number of inversion iterations, the statistic constructed based on the sample mean and sample standard deviation follows the t-distribution rather than the normal distribution. Therefore, the t-distribution is used here to calculate the confidence interval, and its formula is shown in Equation (11). This interval indicates that there is a confidence level of $(1 - \alpha)$ that the true value of the load coefficient is contained

within this range. This method fully considers the additional uncertainty introduced by the sample standard deviation in small-sample estimation, making it more rigorous than the normal distribution assumption.

$$CI = \overline{x} \pm t \cdot \frac{S}{\sqrt{M}} \tag{10}$$

$$t = \frac{\overline{x}_j - \mu_j}{S_j / \sqrt{M}} \tag{11}$$

Next, determine the critical value of the t-distribution: Given the confidence level (95%), find the two-tailed quantile of the t-distribution according to the degree of freedom $df = M - 1$. The essence of the confidence interval is to find an interval such that the probability that the true parameter μ falls within this interval is $1 - \alpha$. According to the properties of the t-distribution, two critical values $-t\left\{\frac{\alpha}{2}, df\right\}$ and $t\left\{\frac{\alpha}{2}, df\right\}$ can be found, satisfying

$$P\left(-t\left\{\frac{\alpha}{2}, df\right\} < t < t\left\{\frac{\alpha}{2}, df\right\}\right) = 1 - \alpha \tag{12}$$

Substitute the definition of the t-statistic into Equation (17) to obtain Equation (12):

$$P\left(-t\left\{\frac{\alpha}{2}, df\right\} < \frac{\overline{x} - \mu}{S/\sqrt{M}} < t\left\{\frac{\alpha}{2}, df\right\}\right) = 1 - \alpha \tag{13}$$

Perform equivalent transformation on the inequality in the above equation to solve for μ:

$$P\left(\overline{x} - t\left\{\frac{\alpha}{2}, df\right\} \cdot \frac{S}{\sqrt{M}} < \mu < \overline{x} + t\left\{\frac{\alpha}{2}, df\right\} \cdot \frac{S}{\sqrt{M}}\right) = 1 - \alpha \tag{14}$$

The confidence interval is obtained as shown in Equation (15):

$$CI = \overline{x} \pm t\left\{\frac{\alpha}{2}, df\right\} \cdot \frac{S}{\sqrt{M}} \tag{15}$$

2.3. Establishment of Physics-Informed Neural Network Model

First, set the main network part of the PINN model, which consists of three parts: input layer, hidden layer(s), and output layer. The input layer has 9 nodes, corresponding to the load coefficients of 9 working conditions applied to the 3D numerical model. The output layer has 108 nodes, corresponding to 6 stress component data of 18 measuring points. Perform data preprocessing and apply Z-score normalization to the training data. According to the empirical formula, the number of hidden layer nodes is determined to be 15.

Next, set the physical network part of the PINN model, i.e., define the loss function of the network, which includes two parts: Data Loss and Physics-informed Loss. The Data Loss is the difference between the stress value predicted by the neural network and the true stress value in the training dataset, and the mean squared error (Equation (1)) is used as the Data Loss. Hooke's law describes the linear relationship between stress and strain in materials, as shown in Equation (16). The elastic matrix can be calculated from the bulk modulus and shear modulus, as shown in Equation (17). The Physics-informed Loss, i.e., the constitutive relation loss (Hooke's law), is specifically set as shown in Equation (18).

$$\sigma = C : \varepsilon_{\text{tensor}} \tag{16}$$

$$C = \begin{bmatrix} K+\frac{3}{4}G & K-\frac{2}{3}G & K-\frac{2}{3}G & 0 & 0 & 0 \\ K-\frac{2}{3}G & K+\frac{3}{4}G & K-\frac{2}{3}G & 0 & 0 & 0 \\ K-\frac{2}{3}G & K-\frac{2}{3}G & K+\frac{3}{4}G & 0 & 0 & 0 \\ 0 & 0 & 0 & G & 0 & 0 \\ 0 & 0 & 0 & 0 & G & 0 \\ 0 & 0 & 0 & 0 & 0 & G \end{bmatrix} \quad (17)$$

$$L_{\text{phy}} = \frac{1}{N}\sum_{i=1}^{N}\left(\frac{\left|\hat{\sigma} - C : \varepsilon^{i}_{\text{tensor}}\right|}{|\hat{\sigma}|+1\times 10^{6}}\right) + \lambda|\hat{\sigma}|^{2}, \lambda = 1\times 10^{-4} \quad (18)$$

where $\varepsilon_{\text{tensor}}$ is the strain tensor, E is the elastic modulus, and μ is Poisson's ratio. 1×10^6 is the normalization constant, which is slightly larger than the maximum possible stress value (~30 MPa) to prevent the denominator from approaching zero; λ is the L2 regularization coefficient, used to suppress model overfitting and prevent the network from outputting excessively large stress, allowing physical constraints and data fitting to be jointly optimized during training.

2.4. Determination and Sensitivity Analysis of Loss Function Weights

The total loss function is composed of a weighted sum of Data Loss and Physics-informed Loss:

$$L = w_{data}L_{data} + w_{phy}L_{phy} \quad (19)$$

where w_{data} and w_{phy} are the weights for the respective loss terms, and typically $w_{data} + w_{phy} = 1$.

In this study, the weights are preliminarily set as w_{data} = 0.7 and w_{phy} = 0.3. This ratio is primarily based on preliminary pre-experiments and the consideration of prioritizing the fitting of observed stress values at measurement points under sparse data conditions, thereby placing greater emphasis on prediction accuracy. The Physics-informed Loss acts as a regularization term to constrain the solution space, preventing overfitting and enhancing generalization capability. Assigning it an appropriate weight of 0.3 allows the effective embedding of constitutive relations without excessively interfering with data fitting, thus balancing the relationship between data fidelity and physical constraints. To further validate the rationality of the weight selection, a sensitivity analysis scheme is designed. By quantifying the impact of different weight combinations on the inversion results, the optimal weight interval can be determined. The specific steps are as follows:

In the two case studies presented in Section 2, multiple weight combinations were tested. For Case 1, the linear elastic model with noise-free data was relatively insensitive to weight changes. Multiple weight combinations could yield high-accuracy solutions, indicating that PINN possesses good robustness in simple systems dominated by strong physical laws. Case 2, the complex geological model, incorporates uncertainties, heterogeneity, and data noise, making it key for examining how to balance "data-driven" and "physics-driven" components. By comparing the inversion accuracy and physical consistency under different weights for this case, the importance of weight selection for solving complex engineering problems can be clarified, providing empirical evidence for the initial weight choice in this study. The algorithm accuracy under different weight combinations is shown in Table 1 below.

In summary, as w_{data} increases from 0.1 to 0.7, the average error of principal stress decreases from 15.78% to a minimum of 9.35%. This indicates that increasing the weight of the data term is crucial for fitting sparse measured data points. When w_{data} continues to increase to 0.8–0.9, the error rises again while the constitutive error also increases. This suggests that excessive bias toward data-driven approaches can easily lead to overfitting and compromise the overall physical rationality of the stress field. The combination

(0.7, 0.3) achieves the global minimum in principal stress error while maintaining stable constitutive error, representing the optimal balance between data accuracy and physical consistency. Future work may explore adaptive weighting strategies to dynamically adjust the contributions of data with varying regional characteristics and confidence levels, as well as physical constraints.

Table 1. Algorithm accuracy under different weight combinations.

(w_{data}, w_{phy})	Average Principal Stress Error (%)	Average Constitutive Error
(0.1, 0.9)	15.78	0.26
(0.2, 0.8)	15.26	0.34
(0.3, 0.7)	14.65	0.45
(0.4, 0.6)	13.58	0.52
(0.5, 0.5)	13.54	0.61
(0.6, 0.4)	10.18	0.45
(0.7, 0.3)	9.35	0.45
(0.8, 0.2)	11.31	0.62
(0.9, 0.1)	10.26	0.54

2.5. Inversion to Obtain Full-Field Stress Distribution

After completing the training of the Physics-Informed Neural Network (PINN), this study adopts the following strategy to achieve high-precision reconstruction of the full-field stress distribution. First, based on the 95% confidence interval calculated in Section 2.2, the uncertainty space of the boundary loads is constructed. Then, within this confidence interval, Monte Carlo random sampling is performed on the boundary conditions to generate a large number of candidate boundary condition combinations. Each set of sampled boundary conditions is input into the trained Physics-Informed Neural Network model, which directly outputs the corresponding stress prediction results.

To evaluate the reliability of each prediction, the relative error between the predicted stress and the measured stress at the observation points is assessed to ensure it is below a fixed threshold. When the PINN-predicted stress field corresponding to a certain sample meets this accuracy requirement, the set of boundary conditions is recorded as the "optimal boundary conditions".

Finally, these optimal boundary conditions are applied to the three-dimensional finite element geological model, and the full-field stress distribution of the geological model is computed in ABAQUS 2022.

3. Case Analysis

To verify the feasibility of the proposed initial in situ stress field inversion and construction method, a program for initial in situ stress field inversion based on PINN is written using MATLAB R2024a. Based on the ABAQUS finite element analysis software, the initial in situ stress fields of two cases are inverted and constructed. Case 1 is a simple 3D layered isotropic linear elastic model, and Case 2 is a practical engineering application of a complex geological body based on the Xingshan Iron Mine.

3.1. Case 1: Simple 3D Layered Isotropic Linear Elastic Model

The design of Case Study 1 aims to validate the fundamental effectiveness of the "physics-constraint embedding" in the PINN algorithm. The model adopts a regular cubic geometry to represent a typical unit scale in engineering. While the layered structure introduces basic material heterogeneity, it avoids the interference of complex geological features such as faults or folds. This simplification helps observe the algorithm's performance under basic physical constraints. Common geotechnical material properties are applied,

and 18 randomly distributed "simulated" monitoring points are arranged to provide spatially discrete yet regionally covering stress information, mimicking the scenario of limited measured data in practical engineering.

3.1.1. Establishment of Numerical Model in ABAQUS

Based on ABAQUS finite element analysis software, a simple 3D layered isotropic linear elastic model is established as shown in Figure 4. Material parameters, boundary conditions, and mesh division are assigned to the model. The overall 3D numerical model has a length of 50 m, width of 50 m, and burial depth of 50 m. Eight-node hexahedral C3D8R elements are used, with a total of 8000 elements and 9261 nodes. In the case design, 18 random points in the calculation area of the model are selected as hypothetical initial in situ stress measuring points. The material properties of the model are shown in Table 2.

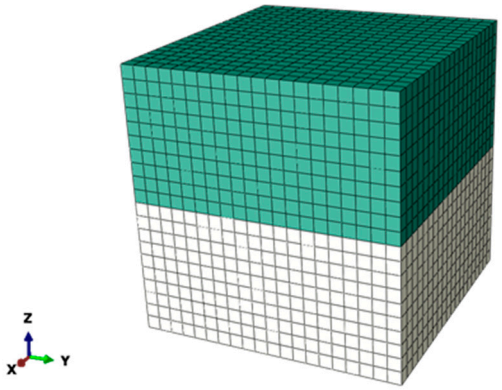

Figure 4. 3D layered isotropic linear elastic numerical model.

Table 2. Material properties of the overall model.

Rock Layer	Density/kg·m^{-3}	Elastic Modulus/GPa	Poisson's Ratio
Layer 1	2800	20	0.25
Layer 2	2500	28	0.21

3.1.2. Determination of Stress Boundary Conditions for the Model

According to the influencing factors of the initial in situ stress field in Section 2.1, 9 types of load forms corresponding to working conditions are applied to the model. A force of 1 MPa is applied to each working condition, and the 9 working conditions are input into ABAQUS for calculation to obtain the stress values at each measuring point. Python (3.9.0) code is written to automatically extract the 6 stress component values of the specified element IDs from the OBD file of ABAQUS, obtaining the stress values at each measuring point under unit load.

3.1.3. Measured Stress Values

In ABAQUS, the loads shown in Table 3 are applied to the case model, and the stress values of 6 stress components at 18 measuring points shown in Table 4 are calculated. These stress values are used as the measured initial in situ stress values at each measuring point to verify the accuracy of the stress values predicted by the algorithm.

Table 3. Loads applied to calculate measured in situ stress values at each measuring point.

Working Condition	Condition 1	Condition 2	Condition 3	Condition 4	Condition 5	Condition 6	Condition 7	Condition 8	Condition 9
Load Value	9.8	3 MPa	3 MPa	3 MPa	3 MPa	1 MPa	1 MPa	1 MPa	1 MPa
Coefficient	9.8	3	3	3	3	1	1	1	1

Table 4. Measured in situ stress values at each measuring point.

Element ID	Measuring Point	Sxx/MPa	Syy/MPa	Szz/MPa	Sxy/MPa	Sxz/MPa	Syz/MPa
1485	1	−4.1655	−4.4481	−2.5629	0.3473	1.2291	−1.5462
1470	2	−3.3904	−3.6406	−1.6996	−0.0053	0.7172	−1.0704
1512	3	−2.5979	−2.7861	−2.1725	−0.0376	0.7978	−1.0941
1377	4	−1.3876	−1.4794	−2.9435	−0.0106	0.6812	−0.5459
3066	5	−4.6967	−3.9242	−2.3805	−0.3457	1.5777	−0.5631
3129	6	−3.5897	−2.4643	−2.5308	−0.4335	2.1713	−0.7130
2893	7	−3.9294	−2.2798	−1.8296	−0.3827	1.3463	−0.3736
2995	8	−1.2680	−1.0595	−3.3443	−0.0297	2.3269	−0.3749
4304	9	−2.2823	−3.2405	−0.2607	−0.0053	−0.0177	−0.0155
4227	10	−2.5087	−3.2496	−0.6087	−0.0047	0.0233	−0.2768
4114	11	−3.8638	−3.8728	−0.3949	0.0132	0.0095	−0.0772
4156	12	−4.4229	−3.5674	−0.2741	0.0234	0.0098	0.0028
5385	13	−2.0995	−2.8978	−0.0265	−0.0345	−0.0224	0.0080
5329	14	−2.7322	−3.0727	−0.1847	−0.0262	−0.0514	0.0400
5452	15	−3.4375	−3.4895	−0.6017	0.0351	0.2070	−0.3144
6606	16	−3.2489	−2.1307	−1.0103	−0.1942	0.4624	−0.0724
6630	17	−3.5606	−2.6201	−0.9441	−0.3171	0.4333	−0.0999
6673	18	−3.7801	−3.0045	−0.7787	−0.2246	0.3399	−0.0887

3.1.4. Determination of Confidence Intervals for Load Coefficients of Each Working Condition Using Bayesian Linear Regression Method

The load coefficients of each working condition and their 95% confidence intervals are finally obtained using the Bayesian linear regression method in Section 2.2.1. The posterior distribution results of each working condition coefficient are shown in Figure 5.

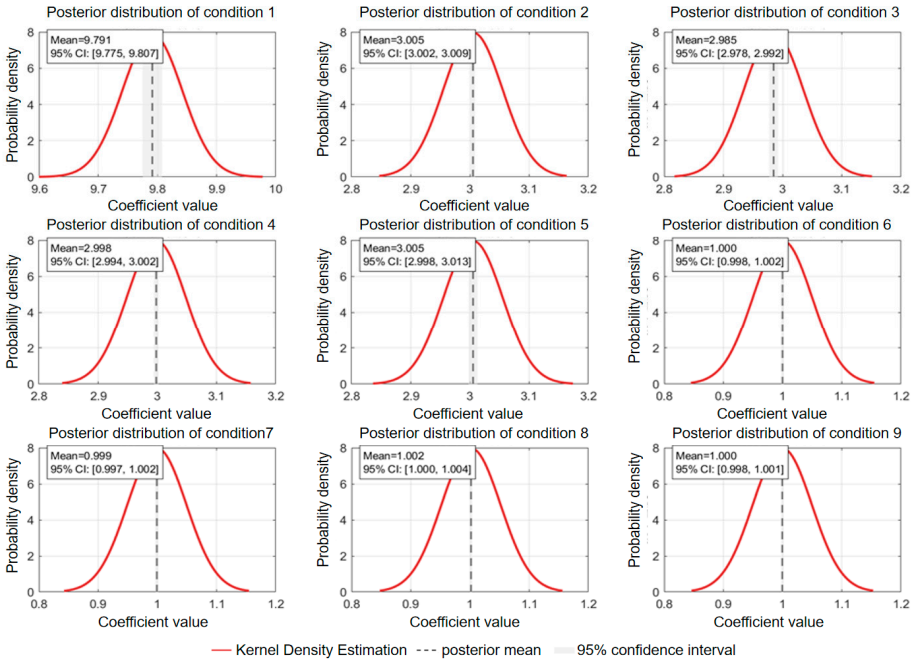

Figure 5. Posterior distribution results of each working condition coefficient.

3.1.5. In Situ Stress Field Inversion Algorithm Based on Physics-Informed Neural Network (PINN)

Dataset Preparation

Based on the above Bayesian linear regression results, 50 groups of load coefficient samples are randomly constructed within the confidence interval using the uniform design method. These samples are input into ABAQUS for calculation to obtain 50 groups of 6 stress component values and 6 strain component values at 18 measuring points. The first 45 groups of data are used as training samples, and the last 5 groups are used as test samples to establish the PINN.

Analysis of Training Results

In Case Study 1, ABAQUS simulation to build the training set takes about 9000 s (50 sets of samples, about 50 s per set). Determining the confidence interval takes about 120 s, and the PINN training time is 58.19 s, with a total computational cost of about 2678 s (0.75 h). The variation in the loss curve during the training process is shown in Figure 6, and the comparison between the predicted stress and the measured stress obtained at the end of training is presented in Table 5 (due to space limitations, only the training results of the first 3 measuring points are listed).

Table 5. Training results of the Physics-Informed Neural Network in Case 1.

Measuring Point	Stress Component	Measured Value (MPa)	Predicted Value (MPa)	Error Percentage (%)	Constitutive Relation Error	Conforms to Elastic Constitutive Relation?
1	Sxx	−4.1655	−4.1658	0.0073	0.00018	Yes
	Syy	−4.4481	−4.4483	0.0053	0.00018	Yes
	Szz	−2.5629	−2.5629	0.0002	0.00018	Yes
	Sxy	0.3473	0.3474	0.0307	0.00018	Yes
	Sxz	1.2291	1.2295	0.0263	0.00018	Yes
	Syz	−1.5462	−1.5456	0.0402	0.00018	Yes
2	Sxx	−3.3904	−3.3891	0.0400	0.00099	Yes
	Syy	−3.6406	−3.6412	0.0157	0.00099	Yes
	Szz	−1.6996	−1.7000	0.0204	0.00099	Yes
	Sxy	−0.0053	−0.0053	0.4568	0.00099	Yes
	Sxz	0.7172	0.7173	0.0165	0.00099	Yes
	Syz	−1.0704	−1.0699	0.0469	0.00099	Yes
3	Sxx	−2.5979	−2.5977	0.0105	0.00028	Yes
	Syy	−2.7861	−2.7852	0.0353	0.00028	Yes
	Szz	−2.1725	−2.1728	0.0108	0.00028	Yes
	Sxy	−0.0376	−0.0376	0.0593	0.00028	Yes
	Sxz	0.7978	0.7974	0.0422	0.00028	Yes
	Syz	−1.0941	−1.0940	0.0080	0.00028	Yes
…	…	…	…	…	…	…

The prediction accuracy is evaluated using the mean absolute relative error (MARE), defined as in Equation (20).

$$MARE = \frac{1}{N}\sum_{i=1}^{N}\left|\frac{y_i^{pred} - y_i^{true}}{y_i^{true}}\right| \times 100\% \quad (20)$$

where y_i^{true} and y_i^{pred} are the true and predicted stress components, respectively, and N is the total number of data points.

From the stress result analysis, the mean absolute relative error of the stress field inverted by the PINN is 0.0772%, with a maximum error of 3.1117% and a minimum error of 0.00016%. All inversion results fall within a reasonable range, and the stress distribution

conforms to basic laws. The average error of the constitutive relation is 0.00077, and all results conform to the elastic constitutive relation set in the 3D numerical model.

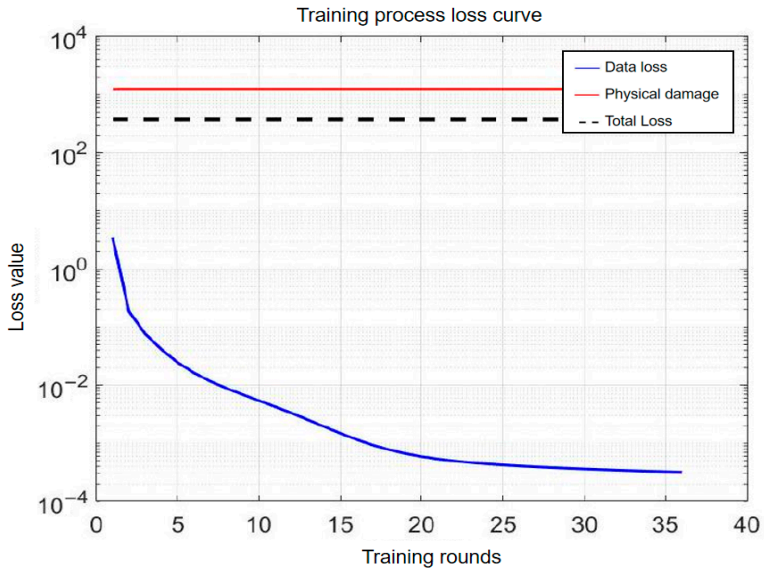

Figure 6. Loss curve of the PINN during training.

To further demonstrate the superiority of the PINN algorithm, the same dataset is used to compare the calculation results of the traditional BP neural network algorithm [37] and the multiple linear regression inversion algorithm [38], as shown in Table 6. Among the three inversion algorithms, the multiple linear regression method has the worst inversion accuracy, with a maximum error percentage of up to 34.95%. The accuracy of the PINN algorithm and the BP neural network algorithm is relatively close, but both the minimum and maximum error percentages of the PINN algorithm are smaller than those of the BP neural network algorithm.

Table 6. Comparison of three inversion methods in Case 1.

Inversion Method	Physics-Informed Neural Network Algorithm		BP Neural Network Algorithm	Multiple Linear Regression
	Data Error	Constitutive Error		
Maximum Error Percentage (%)	3.1117	0.005529	3.4844	34.9474
Minimum Error Percentage (%)	0.00016	0.000183	0.00024	0.00041
Average Error Percentage (%)	0.0772	0.000772	0.0607	0.8278

In in situ stress field inversion, there is a fundamental contradiction between data sparsity and the accuracy and stability of inversion results. Traditional pure data-driven neural network methods rely heavily on a large number of high-quality training samples and have poor generalization ability in scenarios with scarce samples. By embedding the rock constitutive relation as a constraint into the loss function, PINN introduces a strong physical information regularization effect, which significantly reduces the dependence on the number of training samples and ensures that the inversion results strictly follow physical laws even when data is scarce.

To quantitatively evaluate this advantage, 20 groups of load coefficient samples are also randomly constructed within the confidence interval using the uniform design method. These samples are input into ABAQUS for calculation to obtain 20 groups of 6 stress component values and 6 strain component values at 18 measuring points. The first 15 groups of data are used as training samples, and the last 5 groups are used as test samples. These samples are respectively input into the PINN algorithm and the BP neural network for

training, and the training results are compared with those of 50 groups of training samples, as shown in Table 7. When the number of training samples is 50 groups, both the PINN and the BP neural network can achieve good inversion accuracy. When the number of samples is reduced to 20 groups, the maximum inversion error of the PINN increases to 15.67%, with an average error of 0.299%, and its constitutive residual still remains at a low level of 0.027% and 0.0030%. This indicates that although the absolute accuracy decreases due to scarce data, its solution is always effectively constrained within a reasonable constitutive relation. For the BP neural network, the maximum error increases to 31.07%, and the average error (0.423%) is also significantly higher than that of the PINN. This is because without physical constraints, the network is highly prone to overfitting to sparse noise data, affecting inversion accuracy. Through the above data comparison, it is strongly proved that the PINN method, relying on its physical constraint advantage, demonstrates excellent data utilization efficiency and inversion robustness under scarce sample conditions. Therefore, for in situ stress inversion problems with high exploration costs and extremely limited measuring point data, the PINN provides a highly reliable and cost-effective solution.

Table 7. Comparison of training results between 50 groups and 20 groups of training samples in Case 1.

Inversion Method	Physics-Informed Neural Network Algorithm				BP Neural Network Algorithm	
Number of Groups	50 Groups		20 Groups		50 Groups	20 Groups
	Data Error	Constitutive Error	Data Error	Constitutive Error		
Maximum Error Percentage (%)	3.1117	0.005529	15.6668	0.02684	3.4844	31.05776
Minimum Error Percentage (%)	0.00016	0.000183	0.00196	0.000185	0.00024	0.00125
Average Error Percentage (%)	0.0772	0.000772	0.29914	0.00299	0.0607	0.42274

3.2. Case 2: Practical Engineering Application of Complex Geological Bodies

This case takes the Xingshan Iron Mine as the background and applies the PINN algorithm to invert and reconstruct the 3D in situ stress field of the complex geological body in the mining area. The aim is to verify the effectiveness of the PINN algorithm when applied to complex geological bodies and provide a theoretical basis for mine development and stability evaluation.

3.2.1. Establishment of Numerical Model in ABAQUS

According to the existing AutoCAD 2020 design plan, exploration line geological section map, and other data of the Xingshan Iron Mine, combined with the spatial position of the engineering in situ stress measuring points, the scope of the numerical calculation model for in situ stress field inversion is determined as shown in Figure 7. The Y-direction of the model is along the north direction, the X-direction ranges from 503,100 m to 504,100 m, the Y-direction ranges from 4,422,300 m to 4,423,300 m, and the Z-direction ranges from the ground surface down to −640 m.

The model is meshed as shown in Figure 8. The mesh is refined at the middle ore body and fault, using the free meshing method. Tetrahedral elements with four nodes are used, with a total of 170,864 nodes and 883,963 elements. For the calculation of this model, the fault is treated with weak material properties. The material properties of the three materials in the model are shown in Table 8.

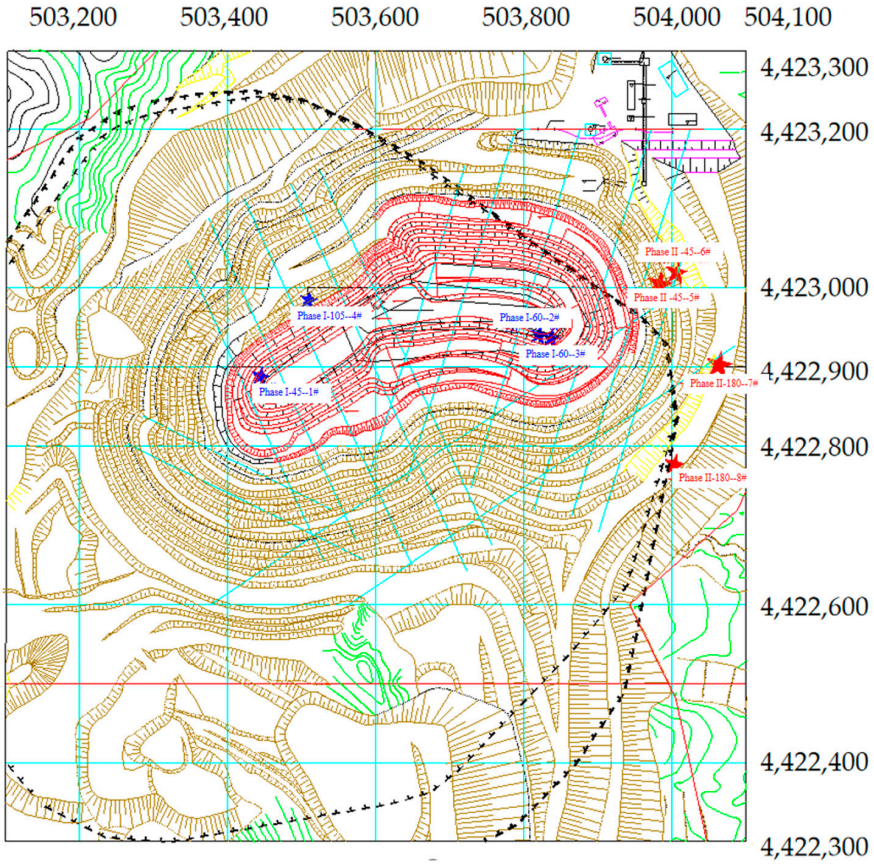

Figure 7. Top view of the modeling scope of the mining area.

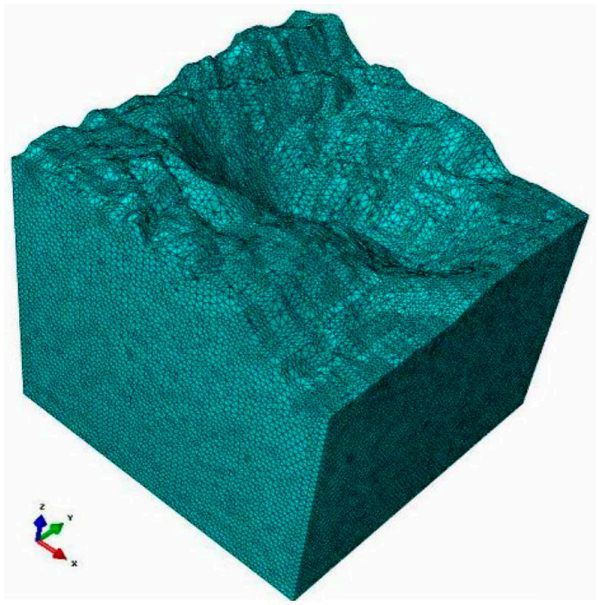

Figure 8. Mesh division of the model in Case 2.

Table 8. Material properties of the complex geological model.

Name	Density/kg·m^{-3}	Elastic Modulus/GPa	Poisson's Ratio
Rock Mass	2620	7.4	0.27
Ore Body	3710	10	0.20
Fault	2600	1.96	0.35

3.2.2. Determination of Stress Boundary Conditions for the Model

As in Section 3.1.2, 9 working conditions are also applied to this complex geological model.

3.2.3. Measured Stress Values

Using the hollow inclusion stress relief method, the University of Science and Technology Beijing conducted in situ stress measurements at the Xingshan Iron Mine, obtaining data from a total of 8 monitoring points. To perform the in situ stress inversion, these measurements were converted into three normal stresses and three shear stresses. The final stress components at each monitoring point are presented in Table 9.

Table 9. Measured in situ stress values at each measuring point in Case 2.

Element ID	Measuring Point	Sxx/MPa	Syy/MPa	Szz/MPa	Sxy/MPa	Sxz/MPa	Syz/MPa
197401	1	−4.6531	−3.6262	−1.4643	−0.9362	−0.3150	−0.6806
172803	2	−5.3904	−3.0678	−2.0561	0.3674	−0.4692	1.3971
136313	3	−5.4195	−3.1353	−2.0614	0.5586	−0.4819	1.4127
76768	4	−6.7900	−5.3415	−4.7416	1.0318	−0.0560	0.0708
26540	5	−8.5579	−4.7897	−5.7431	−0.4331	−0.0112	−0.0938
23243	6	−7.2812	−5.5145	−5.4011	−0.2747	−0.1106	−1.1747
22954	7	−15.2795	−8.6554	−8.9938	−0.6584	−0.0267	−0.1551
3229	8	−9.3149	−8.9030	−13.6592	0.0821	−1.2167	0.8834

3.2.4. Determination of Confidence Intervals for Load Coefficients of Each Working Condition Using Bayesian Linear Regression Method

The posterior distribution results of the coefficients under each working condition, obtained using the Bayesian linear regression method described in Section 2.2.1, are shown in Figure 9.

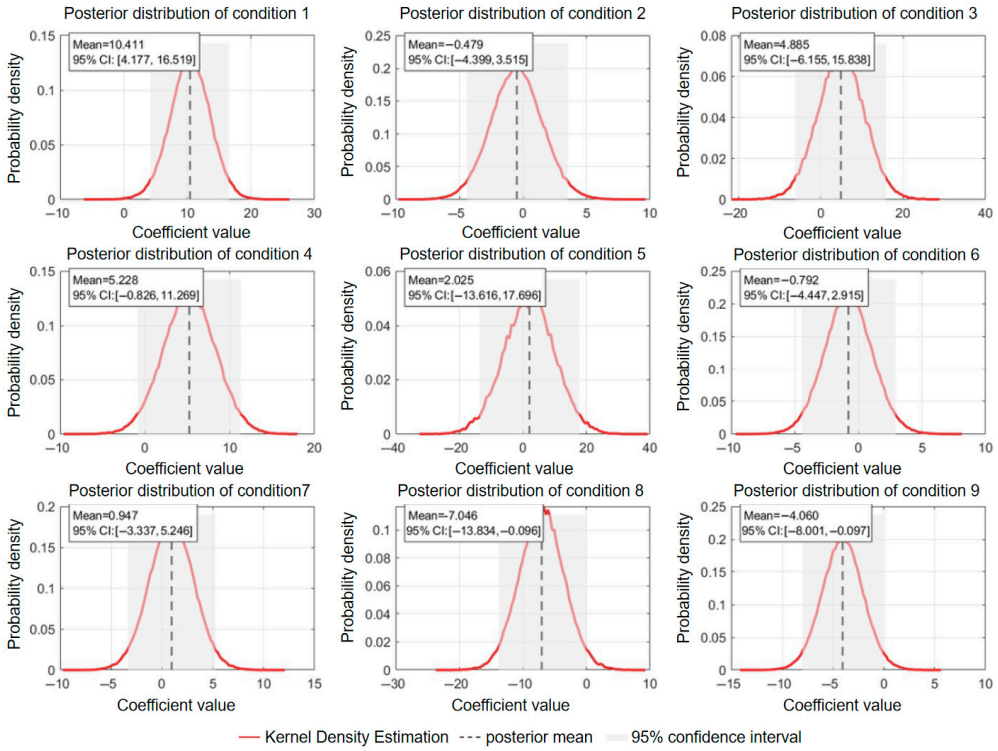

Figure 9. Figure of the posterior distribution results of each operating condition coefficient in Example 2.

Comparing the confidence interval results from Bayesian linear regression in Case 1 and Case 2, it can be observed that the simple idealized model in Case 1 yields precise confidence intervals, whereas the complex geological model in Case 2 exhibits significantly broader confidence intervals. This observation profoundly reveals the intrinsic relationship between model complexity and solution uncertainty in engineering inverse problems. In the uniform linear elastic model, stress transmission paths are clear and unique, allowing the inversion to precisely identify an optimal set of parameters. In contrast, the complex geological model, through the Bayesian probabilistic framework, reveals multiple uncertainties, such as model idealization errors, nonlinear constitutive relationships of geological bodies, noise in measured data, and multicollinearity among responses to different load conditions. The complex geological model incorporates discontinuities such as faults, irregular ore bodies, and contact zones between rock masses, which alter the propagation paths of the regional stress field. Under the same set of boundary loads, multiple internal stress transmission and distribution mechanisms may produce similar stress states at observation points. This multiplicity of stress responses manifests statistically as dispersion in the posterior distribution of load coefficients, leading to broader confidence intervals. However, this result more authentically reflects the inherently ill-posed nature of the inversion problem—namely, that multiple different parameter combinations can explain the observed data with high probability.

Given the high computational cost of complex models, it is difficult to directly apply them to optimization processes that require a large number of iterations. Therefore, this paper introduces the surrogate model optimization method in Section 2.2.2. By constructing a low-cost surrogate of the complex physical model using a neural network, the key nonlinear characteristics are retained while greatly accelerating the optimization iteration and sampling process, aiming to efficiently achieve uncertainty quantification. The core of this method is to generate an "optimal solution set" through multiple optimization iterations, treat this set as statistical samples, and then calculate the confidence interval for each working condition coefficient based on the t-distribution.

3.2.5. Determination of Confidence Intervals for Load Coefficients of Each Working Condition Using Surrogate Model Optimization Method

The load coefficients of each working condition and their 95% confidence intervals finally obtained using the surrogate model optimization method in Section 2.2.2 are shown in Table 10. The optimization process of each working condition coefficient is shown in Figure 10. It can be seen that during the coefficient optimization process of Working Condition 5, the coefficient fluctuates significantly in the early stage and then stabilizes. The load form of Working Condition 5 is applying triangular compressive stress on the rear side interface of the model. During the learning process of the surrogate model, the initial samples may not fully cover the effective range of Working Condition 5, resulting in the model failing to accurately learn its influence in the early iterations, thus causing fluctuations in the optimization process. As adaptive sampling continuously adds new high-precision samples to the training set, the prediction ability of the surrogate model is continuously improved, and the coefficient of Working Condition 5 is adjusted accordingly and tends to be stable. In addition, multicollinearity between load working conditions is another main reason for coefficient fluctuations. The Bayesian inversion results show that the 95% confidence interval of Working Condition 5 is extremely wide [−13.616, 17.696] and includes zero, indicating that its stress response pattern has "multicollinearity" or significant correlation with other working conditions (e.g., Working Condition 4). During the optimization process, the genetic algorithm finds multiple sets of different coefficient combinations that can achieve similar fitting goodness, leading to the coefficient of Working Condition 5 exploring within the solution space, manifested as large fluctuations.

Table 10. Load factors under various working conditions in Example 2 and their 95% confidence interval results.

Working Condition	Load Coefficient	95% Confidence Interval
1	11.1977	[10.8324, 11.1303]
2	0.3048	[0.4377, 0.6368]
3	6.1049	[4.7311, 5.4953]
4	3.8441	[4.9795, 5.9687]
5	5.8449	[0.3930, 3.1881]
6	−0.1268	[−0.1500, 0.0362]
7	1.1344	[1.1422, 1.3964]
8	−4.9649	[−4.8586, −4.7201]
9	−4.6498	[−4.1394, −3.8150]

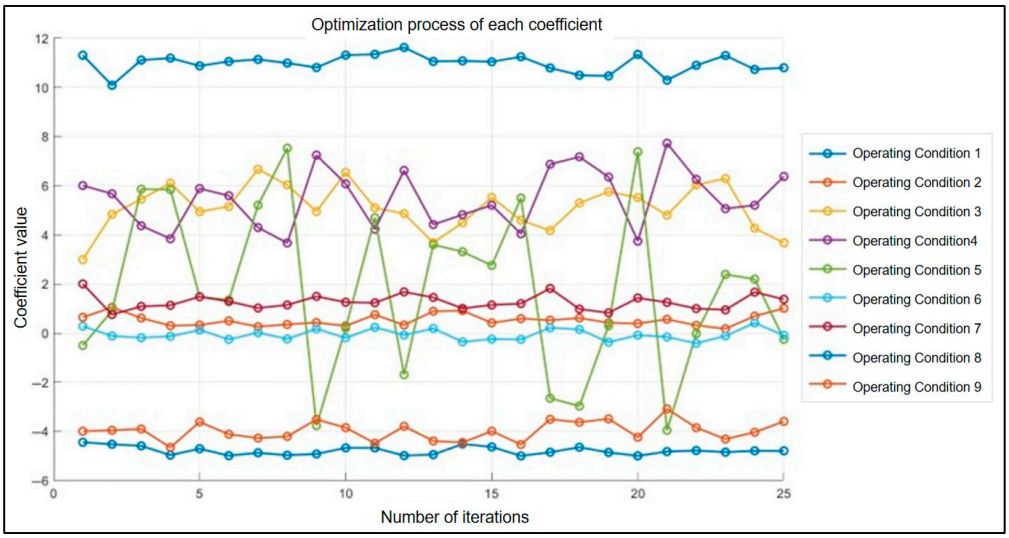

Figure 10. Optimization process of various operating condition coefficientsin Case 2.

This phenomenon also warns us that any single "optimal solution" may only be a special case among many possible solutions. We must shift the inversion result from pursuing an "accurate solution" to grasping a "credible interval". Any engineering decision based on such inversion results must fully consider the most unfavorable effects of all possible working condition combinations near the optimal solution and conduct sensitivity analysis. Only by acknowledging cognitive limitations can reliable engineering designs be made.

3.2.6. In Situ Stress Field Inversion Algorithm Based on Physics-Informed Neural Network (PINN)

Dataset Preparation

Based on the optimization results of the above surrogate model, 50 sets of load factor samples were randomly generated within the confidence interval and input into ABAQUS for calculation, resulting in 50 sets of 6 stress components and 6 strain components at 8 measurement points. The first 45 sets of data were used as training samples, and the last 5 sets were used as test samples. Some of the training samples are shown in Table 11, and the test samples are shown in Table 12, in order to establish the Physics-Informed Neural Network.

Table 11. Training samples of the Physics-Informed Neural Network in Case 2.

Training Group	Gravity Correction Coefficient	Sxx/MPa	Syy/MPa	Szz/MPa	Sxy/MPa	Sxz/MPa	Syz/MPa
1	11.005	−6.2959	−3.8864	−9.2253	−0.6134	−0.4767	−0.1559
2	10.840	−7.1819	−4.0412	−9.1132	−0.6175	−0.4189	−0.1808
3	11.035	−5.7023	−3.8240	−9.2352	−0.6195	−0.5021	−0.1634
4	11.111	−5.9558	−3.7872	−9.2727	−0.6268	−0.4606	−0.1765
5	10.862	−7.2461	−3.7446	−9.0939	−0.6195	−0.4049	−0.2211
…	…	…	…	…	…	…	…

Table 12. Test samples of the Physics-Informed Neural Network in Case 2.

Test Group	Gravity Correction Coefficient	Sxx/MPa	Syy/MPa	Szz/MPa	Sxy/MPa	Sxz/MPa	Syz/MPa
1	10.939	−5.9268	−3.8741	−9.1698	−0.6226	−0.5016	−0.1473
2	11.086	−6.4362	−3.7310	−9.2660	−0.6241	−0.4740	−0.1762
3	10.957	−7.4816	−3.9766	−9.1908	−0.6222	−0.4241	−0.1617
4	10.901	−6.5724	−4.0164	−9.1776	−0.6112	−0.5063	−0.1168
5	11.017	−6.8895	−3.8627	−9.1977	−0.6318	−0.4048	−0.1895
…	…	…	…	…	…	…	…

Analysis of Training Results

For Case Study 2, ABAQUS simulation to build the training set takes about 9000 s (50 sets of samples, about 180 s per set). Determining the confidence interval takes about 300 s, and the PINN training time is 602.81 s, with a total computational cost of about 10,000 s (2.75 h). The computational task was primarily handled by the CPU, with a hardware configuration consisting of an AMD Ryzen 9 7940HX processor and 16.34 GB of total system memory. Among this, neural network training accounted for 596.03 s, representing 98.9% of the total time, indicating relatively high computational efficiency. The variation in the loss curve during the training process is shown in Figure 11, and the comparison between the predicted stress and measured stress obtained at the end of training is presented in Table 13.

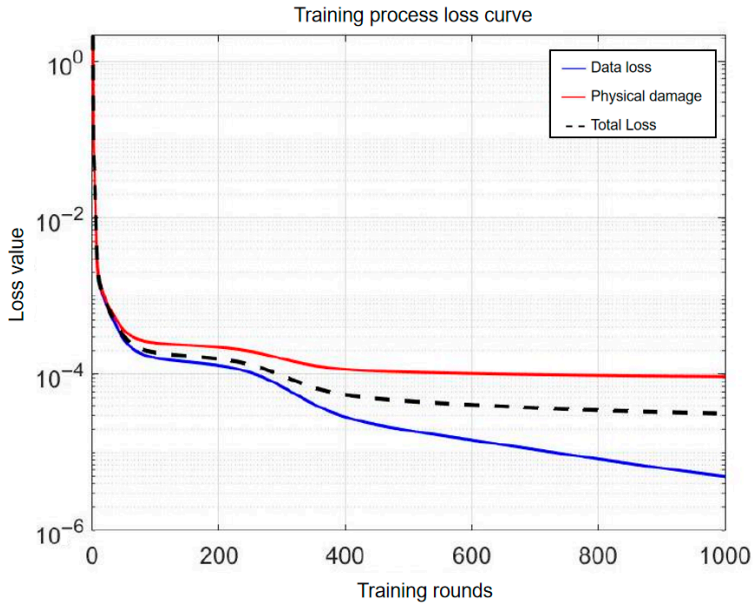

Figure 11. Loss curve of the PINN during training in Case 2.

Table 13. Some training results of the Physics-Informed Neural Network in Case 2.

Measuring Point	Stress Component	Measured Value (MPa)	Predicted Value (MPa)	Error Percentage (%)	Constitutive Relation Error	Conforms to Elastic Constitutive Relation?
1	Sxx	−4.6531	−5.7149	22.82	0.1377	Yes
	Syy	−3.6262	−3.6593	0.91	0.1377	Yes
	Szz	−1.4643	−1.0680	26.06	0.1377	Yes
	Sxy	−0.9362	−1.0278	9.78	0.1377	Yes
	Sxz	−0.3150	−0.3216	2.11	0.1377	Yes
	Syz	−0.6806	−0.6870	0.94	0.1377	Yes
2	Sxx	−5.3904	−6.1362	13.84	0.1560	Yes
	Syy	−3.0678	−3.2670	6.49	0.1560	Yes
	Szz	−2.0561	−1.7216	16.27	0.1560	Yes
	Sxy	0.3674	0.4376	19.10	0.1560	Yes
	Sxz	−0.4692	−0.3737	20.35	0.1560	Yes
	Syz	1.3971	1.6422	17.54	0.1560	Yes
3	Sxx	−5.4195	−5.8002	7.02	0.0648	Yes
	Syy	−3.1353	−3.2497	3.65	0.0648	Yes
	Szz	−2.0614	−2.1293	3.29	0.0648	Yes
	Sxy	0.5586	0.5930	6.16	0.0648	Yes
	Sxz	−0.4819	−0.5308	10.15	0.0648	Yes
	Syz	1.4127	1.5344	8.62	0.0648	Yes
4	Sxx	−6.7900	−7.6157	12.16	1.5251	Yes
	Syy	−5.3415	−5.3779	0.68	1.5251	Yes
	Szz	−4.7416	−4.7606	0.40	1.5251	Yes
	Sxy	1.0318	1.2603	22.14	1.5251	Yes
	Sxz	−0.0560	0.1376	345.79	1.5251	Yes
	Syz	0.0708	0.4488	533.91	1.5251	Yes
…	…	…	…	…	…	…

Analysis of the stress results shows that the mean error of the principal stresses derived from the PINN-based inversion was 9.35%, with a minimum error of 0.137%. All inversion results fell within reasonable ranges, and the stress distribution followed fundamental physical laws. The mean constitutive relationship error was 0.453, consistent with the constitutive model set in the three-dimensional numerical simulation. The number of actual measurement points was sufficient to ensure the stability of the inversion.

As can be seen from Table 13, the errors in horizontal and vertical stresses are relatively small, with the minimum error reaching 0.138%. However, the shear stress error at measurement point 4 is relatively large. The reasons for this are analyzed as follows: (1) It is related to the location of the measurement point. The point is situated within the influence zone of the fault fracture zone. The fundamental contradiction between the discontinuous mechanical behavior of the fault zone and the PINN framework based on continuum linear elastic theory leads to errors. Nonlinear shear behaviors in actual rock masses caused by joints, fractures, and other discontinuities cannot be adequately represented by the linear superposition principle. (2) Shear stress itself is difficult to measure directly on-site. The hollow inclusion stress relief method used in the field measures principal stress magnitudes and orientations, and stress components are derived through coordinate transformation calculations, a process that introduces inherent errors. (3) Nonlinear effects in deep rock masses under long-term tectonic stress: once shear stress exceeds the yield strength, plastic deformation occurs. The model does not account for plastic relations, and using linear elasticity to fit nonlinear shear stress–strain behavior inevitably leads to deviations. Time-dependent effects such as rock “dilatancy” and “viscoelasticity” also influence shear stress distribution. Overall, however, the anomalous shear stress value at this point does not affect the inversion accuracy of the principal stresses nor compromise the overall physical

rationality of the stress distribution. Therefore, the inversion results as a whole remain highly credible.

To further demonstrate the superiority of the PINN algorithm, the same dataset is used to compare the calculation results of the traditional BP neural network algorithm and the multiple linear regression inversion algorithm, as shown in Table 14. Among the three inversion algorithms, the multiple linear regression method has the worst inversion accuracy, which is consistent with the conclusion drawn in Case 1. Meanwhile, the PINN algorithm shows obvious accuracy advantages, with errors much lower than those of the BP neural network algorithm and the multiple linear regression method.

Table 14. Comparison of three inversion methods in Case 2.

Inversion Method	Physics-Informed Neural Network Algorithm		BP Neural Network Algorithm	Multiple Linear Regression
	Data Error	Constitutive Error		
Maximum Error Percentage (%)	533.91	1.525	672.39	567.42
Minimum Error Percentage (%)	0.137	0.065	6.7545	4.2506
Average Error Percentage (%)	40.723	0.453	65.85	82.78
Average Principal Stress Error (%)	9.350	0.453	28.451	42.36

3.2.7. Principal Stress Distribution Law of Xingshan Iron Mine in Case 2

The three-directional principal stresses obtained based on the PINN algorithm are shown in Figures 12–14. Comprehensive analysis of the stress contour maps yields the following basic laws of principal stress:

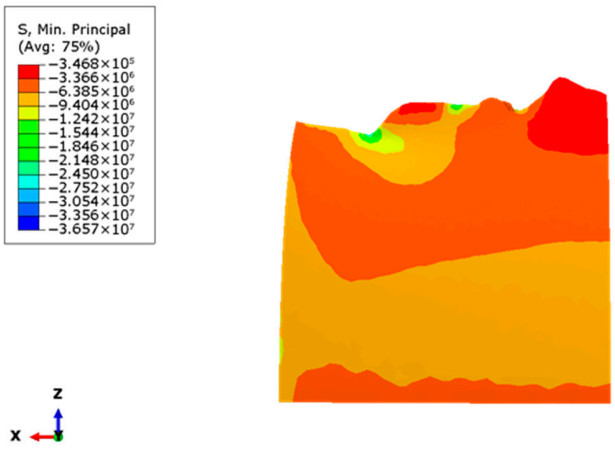

Figure 12. Minimum principal stress contour map of the mine model in Case 2.

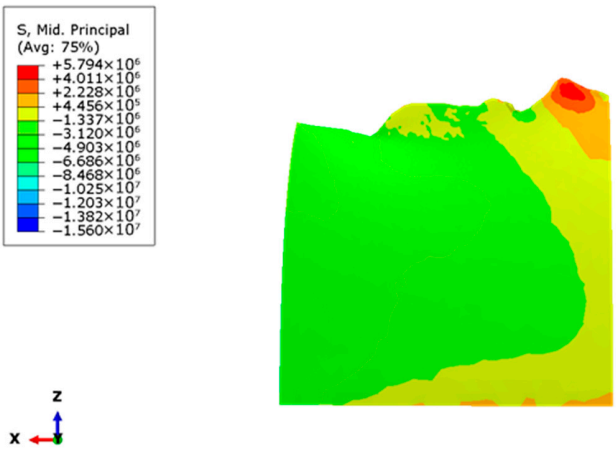

Figure 13. Intermediate principal stress contour map of the mine model in Case 2.

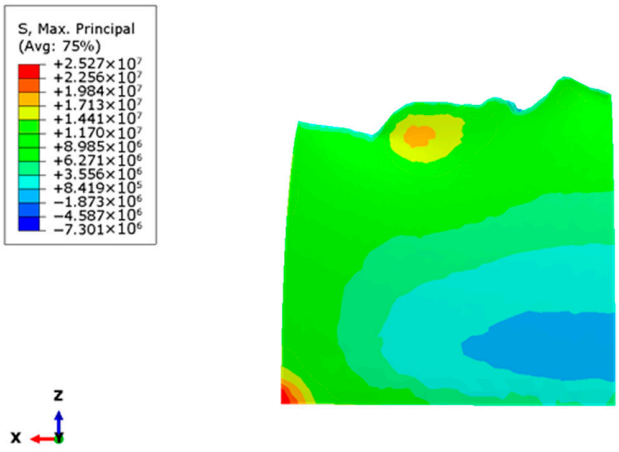

Figure 14. Maximum principal stress contour map of the mine model in Case 2.

The distribution of principal stresses in the calculation area shows that the maximum principal stress ranges from −7.3 MPa to 25.27 MPa, the intermediate principal stress ranges from −15.6 MPa to 5.794 MPa, and the minimum principal stress ranges from −36.57 MPa to −0.347 MPa. Both the maximum and minimum principal stresses increase linearly with depth. The three principal stresses exhibit distinct layering characteristics: As depth increases, the contour lines of the minimum principal stress gradually shift to a horizontal orientation and show a linear correlation with burial depth, indicating that it is primarily controlled by self-weight stress. In contrast, the contour lines of the maximum principal stress gradually shift to a vertical orientation, forming an arched distribution at the bottom, reflecting that it is mainly influenced by horizontal tectonic effects. The in situ stress level across the entire area is affected by the mechanical properties of the rock layers: the greater the elastic modulus and the harder the rock layer, the higher the stress stored in the rock mass of that layer. Therefore, the stress within the ore body is higher than that in the surrounding rock, while stress release zones form near faults, resulting in low in situ stress areas.

4. Conclusions and Prospects

4.1. Conclusions

(1) To address the issue that traditional data-driven models may violate mechanical principles, this study developed a physics-constrained inversion method by embedding the linear elastic constitutive equation (Hooke's law) as a soft constraint into the neural network loss function, thereby establishing a refined inversion optimization algorithm for the in situ stress field. Validation shows that even with a 60% reduction in training samples, the PINN-based inversion still strictly adheres to the constitutive relations.

(2) By analyzing the influencing factors of the in situ stress field, two methods—Bayesian linear regression and surrogate model optimization—were employed to calculate the 95% confidence intervals of the load condition coefficients for the geological model. In Case 1, involving a simple three-dimensional linear elastic model, Bayesian linear regression yielded relatively precise intervals. However, in Case 2 with a complex geological model, both methods revealed multicollinearity among the responses to different load conditions, and the Bayesian approach resulted in wider confidence intervals, reflecting the ill-posed nature of the inverse problem. In contrast, the surrogate model optimization method preserves key nonlinear characteristics of the model and, through multiple optimization iterations, generates an "optimal solution set." The confidence intervals calculated based on the t-distribution for each load coefficient are more accurate.

(3) Based on ABAQUS finite element analysis software, the accuracy and superiority of PINN for initial in situ stress field inversion were validated through two typical cases: a simple 3D linear elastic model and a practical engineering application involving a complex geological model. In Case 1, the maximum inversion error of PINN was only 3.11%, all predicted stresses strictly satisfied the constitutive relations, and the average constitutive error was 0.00077, overcoming the drawback of traditional data-driven models potentially violating mechanical laws. Moreover, under sparse sample conditions, PINN demonstrated excellent data utilization efficiency and inversion robustness owing to its physical constraints. In Case 2, the average principal stress error inverted by PINN was 9.35%, with a minimum error of 0.137%; all results fell within reasonable ranges, stress distribution followed basic laws, and the average constitutive error was 0.453. Compared with traditional BP neural networks and multiple linear regression methods, PINN showed significantly higher prediction accuracy.

It is worth noting that the Physics-Informed Neural Network (PINN) algorithm employed in this study is "not intended to replace" finite element inversion methods. The core advantage of the PINN algorithm lies in its "data–physics fusion paradigm": it embeds the governing equations directly into the network loss function as constraints. Guided by physical laws, the optimal boundary conditions are determined within confidence intervals using only a small number of observation points, which are then imported into finite element forward simulations to obtain the global stress field. This approach avoids the enormous computational cost incurred in traditional finite element inversions, where time-consuming forward simulations are repeatedly invoked to optimize boundary conditions or material parameters.

4.2. Limitation

Although the proposed Physics-Informed Neural Network framework demonstrates good accuracy and physical consistency in in situ stress field inversion, some important limitations remain:

(1) Simplified constitutive assumption: The current PINN framework is based on a linear elastic constitutive model. This choice does not disregard the inherent mechanical complexity of rock masses but rather reflects a staged approach aimed at method validation and algorithmic feasibility. In deep geological settings, rock masses commonly exhibit nonlinear behaviors—such as elastoplastic yielding, damage evolution, time-dependent effects (e.g., creep), and fault slip—under tectonic loading, high confining pressures, and long-term stress histories. Particularly in regions of high stress concentration or geologically weak zones (e.g., fault zones), the stress–strain relationship significantly deviates from linear elasticity. Consequently, a purely linear elastic model cannot adequately capture the true mechanical response.

Therefore, a key direction for future work is to incorporate nonlinear constitutive models into the framework.

(2) Quality and reliability of field measurement data:

The inversion results are highly dependent on the accuracy and spatial distribution of in situ stress measurements. The commonly used hollow inclusion stress relief method has inherent limitations: small errors in the orientation of principal stresses can be amplified during coordinate transformation, leading to substantial inaccuracies in derived shear stress components (e.g., Sxz, Syz). Moreover, stress measurements are typically sparse and confined to borehole sections, making it difficult to resolve local heterogeneities in the three-dimensional stress field. Additional uncertainties arise from measurement noise, instrument drift, and core disturbance during sampling, all of which can compromise the stability and reliability of the inversion.

4.3. Prospects

The three-dimensional numerical model used in this study is based on the linear elastic assumption. Future work will incorporate constitutive relations that better reflect the nonlinear characteristics of in situ stress fields, such as elastoplastic or viscoplastic constitutive constraints. Additionally, research will be conducted on the physical embedding of discontinuous geological features such as faults and folds. Furthermore, in situ stress measurements via drilling in actual mining areas will be carried out to further evaluate the inversion performance under real engineering conditions.

Author Contributions: Conceptualization, F.L., L.W., J.W. and R.Y.; Methodology, F.L., L.W. and Z.L.; Software, Z.L.; Investigation, L.W., J.W. and R.Y.; Resources, Z.L. and C.Z.; Data curation, F.L.; Writing—original draft, L.W.; Visualization, L.W.; Supervision, F.L., Z.L., J.W. and C.Z.; Project administration, F.L., J.W., C.Z. and R.Y.; Funding acquisition, J.W. All authors have read and agreed to the published version of the manuscript.

Funding: This research was funded by the National Natural Science Foundation of China Youth Science Fund (NO. 52404073) and the State Key Laboratory of Deep Coal Mining Response and Disaster Prevention Open Fund (NO. SKLMRDPC23KF02) and the Research Base Construction Project: 'Research on Fine Inversion Algorithm of In-situ Stress Field Based on Physical Information Constraints' (No. FRF-BD-25-056).

Data Availability Statement: The original contributions presented in this study are included in the article. Further inquiries can be directed to the corresponding author.

Conflicts of Interest: The authors declare no conflicts of interest.

References

1. Hudson, J.; Cornet, F.; Christiansson, R. ISRM Suggested Methods for rock stress estimation—Part 1: Strategy for rock stress estimation. *Int. J. Rock Mech. Min. Sci.* **2003**, *40*, 991–998. [CrossRef]
2. Cai, M. Rock Mass Characterization and Rock Property Variability Considerations for Tunnel and Cavern Design. *Rock Mech. Rock Eng.* **2011**, *44*, 379–399. [CrossRef]
3. Latham, J.P.; Xiang, J.; Belayneh, M.; Nick, H.M.; Tsang, C.F.; Blunt, M.J. Modelling stress-dependent permeability in fractured rock including effects of propagating and bending fractures. *Int. J. Rock Mech. Min. Sci.* **2013**, *57*, 100–112. [CrossRef]
4. Ren, H.G.; Tan, Z.Y.; Feng, P.X. Back Analysis of In-Situ Stress under Complicated Geological Conditions Based on Function Superposition of Multiple Regressions. *Eng. Technol. Res.* **2017**, *5*, 157–165. [CrossRef] [PubMed]
5. Jiang, Q.; Feng, X.T.; Xiang, T.B.; Su, G.S. Rockburst characteristics and numerical simulation based on a new energy index: A case study of a tunnel at 2500 m depth. *Bull. Eng. Geol. Environ.* **2010**, *69*, 381–388. [CrossRef]
6. Xie, H.P.; Gao, F.; Ju, Y. Research and exploration on deep rock mechanics. *Chin. J. Rock Mech. Eng.* **2015**, *34*, 2161–2178. (In Chinese)
7. Li, J.; Liu, C.; Liu, H.M.; Xu, Y.; Xie, L.; Huang, G. Distribution Law of In-Situ Stress and Its Influencing Factors in Complex Fault Tectonic Areas. *J. China Univ. Min. Technol.* **2021**, *50*, 123–137.
8. Samui, P. Support vector machine applied to settlement of shallow foundations on cohesionless soils. *Comput. Geotech.* **2007**, *35*, 419–427. [CrossRef]
9. Qian, L.; Yao, T.; Mo, Z.; Zhang, J.; Li, Y.; Zhang, R.; Xu, N.; Li, Z. GAN Inversion Method of an Initial In-Situ Stress Field Based on the Lateral Stress Coefficient. *Sci. Rep.* **2021**, *11*, 21825. [CrossRef] [PubMed]
10. Lyu, F.; Liu, J.; Chen, L.; Tao, B.; Liu, X. 3D in-situ stress prediction for shale reservoirs based on the CapsNet-BiLSTM hybrid model. *Int. J. Rock Mech. Min. Sci.* **2024**, *183*, 105937. [CrossRef]
11. Zhang, P. In-Situ Stress Inversion and Distribution Characteristics of Tunnel Based on Numerical Simulation and Neural Network Technology. *Shock Vib.* **2021**, *2021*, 5545283. [CrossRef]
12. Song, Z.; Jiang, Q.; Chen, P.; Xia, Y.; Xiang, T. Nonlinear Intelligent Inversion Method and Practice for In-situ Stress in Stratified Rock Masses with Deep Valley. *Rock Mech. Rock Eng.* **2024**, *58*, 1933–1955. [CrossRef]
13. McKenzie, D.F. *Cambridge University Press, 1696–1712: A Bibliographical Study*; Cambridge University Press: Cambridge, UK, 2010; Volume 1696–1712.
14. Rutqvist, J. Fractured rock stress-permeability relationships from in situ data and effects of temperature and chemical-mechanical couplings. *Geofluids* **2015**, *15*, 48–66. [CrossRef]

15. Montáns, F.J.; Chinesta, F.; Gómez-Bombarelli, R.; Kutz, J.N. Data-driven modeling and learning in science and engineering. *Comptes Rendus Mécanique* **2019**, *347*, 845–855. [CrossRef]
16. Chen, Y.; Zhang, D. Physics-Constrained Deep Learning of Geomechanical Logs. *IEEE Trans. Geosci. Remote Sens.* **2020**, *58*, 5932–5943. [CrossRef]
17. Raissi, M.; Perdikaris, P.; Karniadakis, E.G. Physics-Informed Neural Networks: A Deep Learning Framework for Solving Forward and Inverse Problems Involving Nonlinear Partial Differential Equations. *J. Comput. Phys.* **2019**, *378*, 686–707. [CrossRef]
18. Cuomo, S.; Di Cola, V.S.; Giampaolo, F.; Rozza, G.; Raissi, M.; Piccialli, F. Scientific machine learning through physics–informed neural networks: Where we are and what's next. *J. Sci. Comput.* **2022**, *92*, 88. [CrossRef]
19. Karniadakis, G.E.; Kevrekidis, I.G.; Lu, L.; Perdikaris, P.; Wang, S.; Yang, L. Physics-informed machine learning. *Nat. Rev. Phys.* **2021**, *3*, 422–440. [CrossRef]
20. Bin Waheed, U.; Haghighat, E.; Alkhalifah, T.; Song, C.; Hao, Q. PINNeik: Eikonal Solution Using Physics-Informed Neural Networks. *Comput. Geosci.* **2021**, *155*, 104833. [CrossRef]
21. Jin, X.; Cai, S.; Li, H.; Karniadakis, G.E. NSFnets (Navier-Stokes flow nets): Physics-informed neural networks for the incompressible Navier-Stokes equations. *J. Comput. Phys.* **2020**, *426*, 109951. [CrossRef]
22. Madir, B.E.; Luddens, F.; Lothodé, C.; Danaila, I. Physics Informed Neural Networks for heat conduction with phase change. *Int. J. Heat Mass Transf.* **2025**, *252*, 127430. [CrossRef]
23. Billah, M.M.; Khan, A.I.; Liu, J.; Dutta, P. Physics-Informed Deep Neural Network for Inverse Heat Transfer Problems in Materials. *Mater. Today Commun.* **2023**, *35*, 106336. [CrossRef]
24. Zhang, Z.; Mao, Y.; Su, X.; Yuan, X. Inversion learning of turbulent thermal diffusion for film cooling. *Phys. Fluids* **2022**, *34*, 035118. [CrossRef]
25. Jalili, D.; Jang, S.; Jadidi, M.; Giustini, G.; Keshmiri, A.; Mahmoudi, Y. Physics-informed neural networks for heat transfer prediction in two-phase flows. *Int. J. Heat Mass Transf.* **2024**, *221*, 125089. [CrossRef]
26. Taufik, H.M.; Huang, X.; Alkhalifah, T. Latent Representation Learning in Physics-Informed Neural Networks for Full Waveform Inversion. *Earth Space Sci.* **2025**, *12*, e2024EA004107. [CrossRef]
27. Chen, Y.; Lu, L.; Karniadakis, G.E.; Dal Negro, L. Physics-informed neural networks for inverse problems in nano-optics and metamaterials. *Opt. Express* **2020**, *28*, 11618–11633. [CrossRef] [PubMed]
28. Haghighat, E.; Raissi, M.; Moure, A.; Gomez, H.; Juanes, R. A physics-informed deep learning framework for inversion and surrogate modeling in solid mechanics. *Comput. Methods Appl. Mech. Eng.* **2021**, *379*, 113741. [CrossRef]
29. Chai, Y.; Chen, Z.; Yin, S. A Preliminary Analysis of In-Situ Stress at Mount Meager by Displacement Discontinuity Method with Topography and Tectonics Considered. *Energies* **2023**, *16*, 1397. [CrossRef]
30. Tan, N.; Yang, R.; Tan, Z. Influence of complicated faults on the differentiation and accumulation of in-situ stress in deep rock mass. *Int. J. Miner. Metall. Mater.* **2023**, *30*, 791–801. [CrossRef]
31. Chu, Y.; Yin, Z.; Yu, K. Bayesian scale mixtures of normals linear regression and Bayesian quantile regression with big data and variable selection. *J. Comput. Appl. Math.* **2023**, *428*, 115192. [CrossRef]
32. Wang, N.; Reformat, M.; Yao, W.; Zhao, Y.; Chen, X. Fuzzy Linear regression based on approximate Bayesian computation. *Appl. Soft Comput. J.* **2020**, *97*, 106763. [CrossRef]
33. Lulusi, L.; Sugiarto, S.; Saleh, S.M.; Isya, M.; Rusdi, M.; Rahma, R. Bayesian MCMC with Gibbs sampling for saturation flow rate estimation in heterogeneous traffic at pretimed signalized intersections. *MethodsX* **2025**, *15*, 103507. [CrossRef] [PubMed]
34. Nguyen, A.; Canning, G.A.; Rioux, R.M.; Janik, M.J. A Markov chain Monte Carlo (MCMC) Bayesian inference approach to analyze apparent activation barriers and reaction orders from microreactor data. *J. Catal.* **2025**, *451*, 116389. [CrossRef]
35. Luo, C.; Lu, W.; Pan, Z.; Bai, Y.; Dong, G. Simultaneous identification of groundwater pollution source and important hydrogeological parameters considering the noise uncertainty of observational data. *Environ. Sci. Pollut. Res.* **2023**, *30*, 84267–84282. [CrossRef] [PubMed]
36. Wang, J.A.; Li, F. Optimization Algorithm for Complex In-Situ Stress Field Inversion and New Research Progress. *J. China Univ. Min. Technol.* **2015**, *44*, 189–205. (In Chinese)
37. Yan, H.C.; Liu, H.Z.; Li, Y.; Zhuo, L.; Xiao, M.L.; Chen, K.P.; Wu, J.M.; Pei, J.L. Inversion Analysis of the In Situ Stress Field around Underground Caverns Based on Particle Swarm Optimization Optimized Back Propagation Neural Network. *Appl. Sci.* **2023**, *13*, 4697. [CrossRef]
38. Liang, J.; Zhu, Q.; Sui, L.; Duan, L.; Wang, D. Research on Elaborate Construction of Complex 3D Geological Model and In-Situ Stress Inversion. *Geotech. Geol. Eng.* **2023**, *42*, 1373–1388. [CrossRef]

Disclaimer/Publisher's Note: The statements, opinions and data contained in all publications are solely those of the individual author(s) and contributor(s) and not of MDPI and/or the editor(s). MDPI and/or the editor(s) disclaim responsibility for any injury to people or property resulting from any ideas, methods, instructions or products referred to in the content.